Electronic Supplementary Material (ESI) for Inorganic Chemistry Frontiers.

Supporting Information

Phosphorus Doping Induced the Co-Construction of Sulfur Vacancies and Heterojunctions in Tin Disulfide as a Durable Anode for Lithium/Sodium-Ion Batteries

Zhen Kong[a,b], Meiling Huang[b], Zhenyan Liang[b], Huayao Tu[b], Kang Zhang[b], Yongliang Shao[a,b], Yongzhong Wu[a,b,*], Xiaopeng Hao[a,b,*]

a. School of Materials Science and Engineering, Qilu University of Technology (Shandong Academy of Science), Jinan, 250353, P. R. China;

b. State Key Lab of Crystal Materials, Shandong University, Jinan 250100, P. R. China.

*Corresponding author: E-mail: wuyz@sdu.edu.cn; xphao@sdu.edu.cn

This file includes:

S1. Materials

All the reagents were purchased from Sinopharm Chemical Reagent Co., Ltd. (Shanghai). All the reagents were used as received.

S2. Experimental Section

S2.1 Preparation of GO: Graphene oxide (GO) was prepared based on the previous reported method[1].

S2.2 Preparation of $Sn_6O_4(OH)_4$: Firstly, 0.5 g of $SnCl_2 \cdot 2H_2O$ was added into 30 ml of ethylenediamine solution followed by ultrasonic dispersion for 30 min to form solution A. Secondly, 0.15 g of NaOH was added into 30 ml aqueous solution and followed by stirring for 5 min to form solution B. Thirdly, Solution B was added into solution A drop by drop under stirring for 1h. Finally, the obtained solution was centrifuged and washed thrice, after dried in a vacuum oven at 60 °C, the $Sn_6O_4(OH)_4$ nanoparticles were obtained.

S2.3 Preparation of SnS_2/GO, $SnS_{2-x}P_x$/RGO and SnS/RGO composites: Firstly, 7 ml (6 mg ml^{-1}) of GO was dispersed into 30 ml of aqueous solution followed by ultrasonic dispersion for 30 min. Secondly, 0.1 g of the obtained $Sn_6O_4(OH)_4$ and 0.12 g of thioacetamide were added into the mixture and followed by ultrasonic dispersion for 20 min. Thirdly, the obtained solution was transferred into a 40 ml teflon-lined stainless-steel autoclave and reacted at 200 °C for 12 h. After cooled to ambient temperature naturally, the obtained power centrifuged and washed thrice, after freeze-drying treatment, the graphene encapsulated SnS_2 nanoplates composite material was obtained, which designated as SnS_2/GO. The as-prepared SnS_2/GO was calcined under

Ar atmosphere with a heating rate of 5 ℃/min using $NaH_2PO_2•2H_2O$ as reducing agent. SnS_2/GO and $NaH_2PO_2•2H_2O$ were placed at two separate positions of the alumina ark with a mass ratio of 1:15 and then heated at 350 ℃ and 550 ℃ for 1 h, respectively. After naturally cooled to room temperature, $SnS_{2-x}P_x$/RGO and SnS/RGO composites material was obtained.

S2.4 Preparation of $NaNi_{0.45}Cu_{0.05}Mn_{0.4}Ti_{0.1}O_2$: The $NaNi_{0.45}Cu_{0.05}Mn_{0.4}Ti_{0.1}O_2$ was based on the previous reported method[2].

S3. Material Characterizations

The crystalline structure of the as-prepared samples was determined by powder X-ray diffraction (XRD, Bruker, D8 Advance X-ray diffractometer, Cu Kα, λ = 1.5406 Å). Hitachi S-4800 field emission scanning electron microscopy (SEM) and a JEM-2100F high-resolution transmission electron microscopy (HRTEM) were used to study the morphology and structure of the samples. Elemental analysis was measured by energy dispersive X-ray spectroscopy (EDS, Horiba EMAX Energy EX-350) equipped in SEM. The thermogravimetric analysis (TGA) was performed with a Mettler Toledo TGA-2 thermal gravimetric analyzer under air atmosphere with a heating rate of 10 °C/min. The X-ray photoelectron spectroscopy (XPS) measurement was carried out using a monochromatized XPS spectrometer (a ThermoFisher ESCALAB 250) with Al (Kα) radiation as the probe. The surface area results were obtained by nitrogen adsorption and desorption isotherms (ASAP 2020 sorptometer). The pore size distributions were determined according to Barrett-Joyner-Halenda (BJH) desorption model. The room-temperature Raman spectra of samples were recorded on a LabRam

HR system from Horiba Jobin Yvon at room temperature using the 532 nm solid laser as the exciting source. Electron paramagnetic resonance (EPR) spectra were obtained from a Bruker EMXplus-10/12 spectrometer at room temperature.

S4. Electrochemical Measurements

The electrodes were fabricated by mixing 80% the active materials, 10% acetylene black, and 10% polyvinylidene difluoride (PVDF) dissolved in N-methyl-2-pyrrolidine (NMP). The mixed slurry uniformly pasted on copper foil and dried at 110 °C under vacuum for 10 h. Electrodes with a diameter of 12 mm and the accurate mass loadings of the active materials were controlled in the range of 0.8-1.2 mg.

For LIBs, 1 M $LiPF_6$ in EC: DMC: EMC (1:1:1, wt%) with 2.0% FEC was utilized as electrolyte. 2032-type coin cells were then assembled in a glove box filled with Ar (oxygen and moisture less than 1 ppm) using polypropylene film (Celgard 2320) as the separator. For the half-cell, pure Li metal was used as the counter electrode. The coin-type full battery was assembled using commercial $LiNi_{0.6}Co_{0.2}Mn_{0.2}O_2$ (NCM622) as the cathode, and 1 M $LiPF_6$ in EC: DMC: EMC (1:1:1, wt%) with 2.0% FEC used as the electrolyte. The cathode electrode was prepared by mixing NCM622, acetylene black, and polyvinylidene fluoride (PVDF) in a weight ratio of 8:1:1, followed by coating on aluminum foil. Prior to full-cell fabrication, the $SnS_{2-x}P_x$/RGO anode was electrochemically activated by prelithiation, which was implemented by cycling it against a Li foil to eliminate the initial irreversible capacity. The mass loading for the cathode and anode was about 6:1. The full-cells of $SnS_{2-x}P_x$/RGO//NCM622 were tested between 2.0 and 4.2 V (vs Li^+/Li) at room temperature.

For the SIBs, Na metal is the counter and reference electrode in the half cells. The glass microfibers of Whatman GF/D acted as the separator and $NaClO_4$ (1.0 M) in ethylene carbonate (EC) and diethyl carbonate (DEC) (volume ratio of 1:1) with 5.0 wt % Fluoroethylene Carbonate (FEC) adding acted as electrolyte. The coin-type full battery was assembled using the prepared $NaNi_{0.45}Cu_{0.05}Mn_{0.4}Ti_{0.1}$ (NaNCMT) as the cathode, and the $SnS_{2-x}P_x$/RGO anode was electrochemically activated by presodiation. The full-cells of $SnS_{2-x}P_x$/RGO//NaNCMT were tested between 2.0 and 4.2 V (vs Na^+/Na) at room temperature.

The charge-discharge tests were performed on a NEWARE battery measurement system between cut off voltages of 3 V and 0.01 V. The obtained specific capacities were calculated based on the total mass of the active materials. Cyclic voltammetry (CV) tests were carried out between 0.01 V and 3 V at different scan rates from 0.1 to 1.0 mV s^{-1} on a CHI760D electrochemical working station. Electrochemical impedance spectroscopy (EIS) patterns were recorded using a CHI760D electrochemical working station in the frequency range from 100 kHz to 0.01 Hz with amplitude of 5 mV.

S5. Supplementary Figures S1-S14

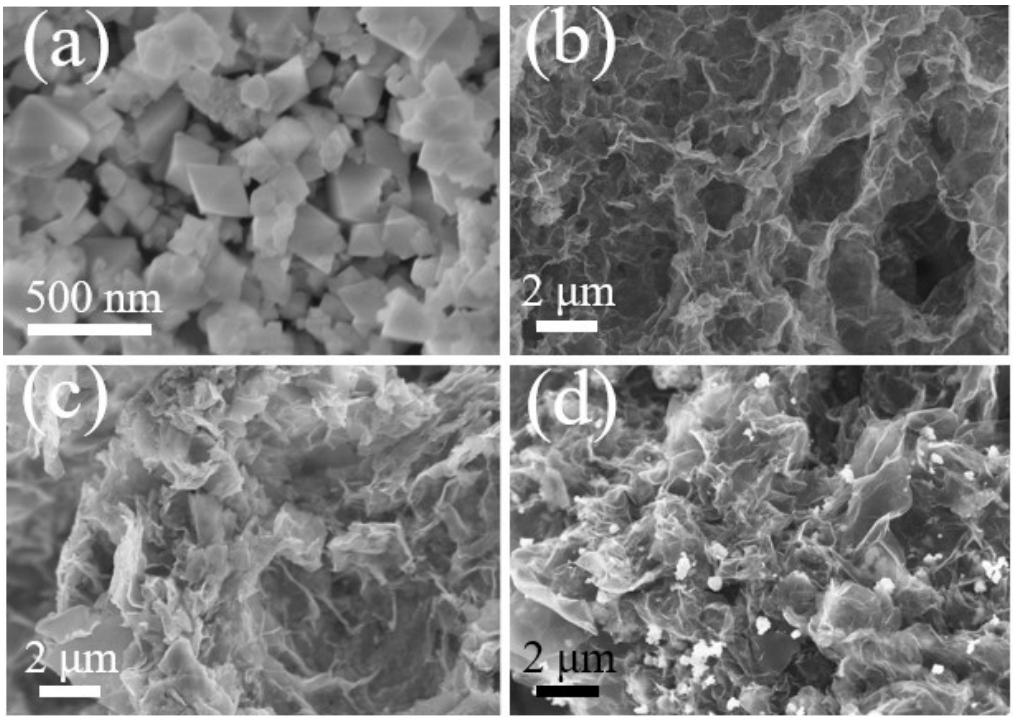

Fig. S1. SEM images of (a) $Sn_6O_4(OH)_4$, (b) SnS_2/GO with $Sn_6O_4(OH)_4$ as tin source and thioacetamide as sulfur source, (c) SnS_2/GO-1 with $SnCl_2{\cdot}2H_2O$ as tin source and thioacetamide as sulfur source and (d) SnS_2/GO-2 with $Sn_6O_4(OH)_4$ as tin source and thiourea as sulfur source.

Fig. S1 shows the SEM images of SnS_2-based composites prepared using different tin and sulfur sources. SnS_2/GO composite using $Sn_6O_4(OH)_4$ nanoparticles as the tin precursor (**Fig. S1**b) displays a 3D porous network morphology and SnS_2 nanoplates encapsulated by graphene, while SnS_2/GO-1 composite with the tin precursor of $SnCl_2{\bullet}2H_2O$ (**Fig. S1**c) shows compact morphology. The sulfur source also has a great impact on the morphology of the SnS_2-based composite. As shown in **Fig. S1**d, the SnS_2/GO-2 composite prepared with thiourea as the sulfur source exists partial agglomeration. The above results show that sulfur and tin sources have a significance influence on the morphology of SnS_2/GO composites.

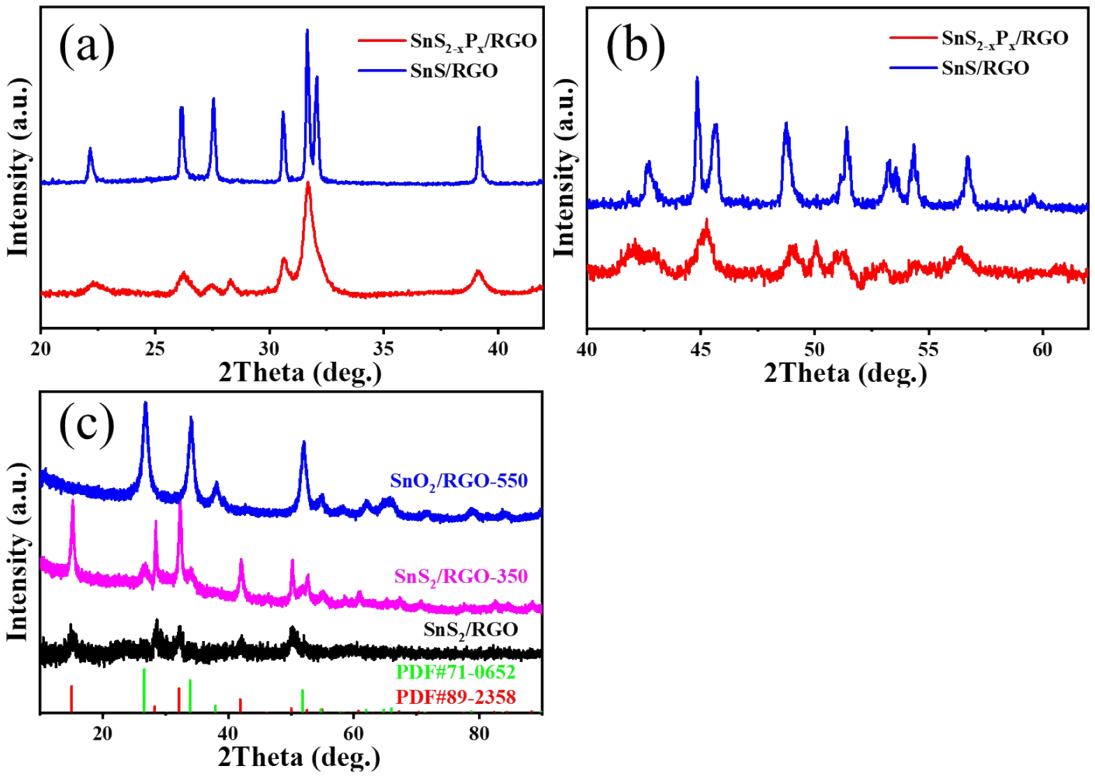

Fig. S2. (a, b) Enlarged view of XRD patterns of samples $SnS_{2-x}P_x$/RGO and SnS/RGO, (c) XRD patterns of SnS_2/GO and corresponding samples calcined at 350 ℃ (SnS_2/GO-350) and 550 ℃ (SnS_2/GO-550).

The sample $SnS_{2-x}P_x$/RGO contains a complex phase, the peaks at 15°, 28° and 50° correspond to the plans of (001), (100) and (110) for SnS_2. The peaks at 22°, 26°, 27.4°and 39° (**Fig. S2**a) corresponding to SnS phase. The peaks between 30-35° (**Fig. S2**a) and 40-65° (**Fig. S2**b) have some difference for the two samples, indicating that $SnS_{2-x}P_x$/RGO is an intermediate state between SnS_2 and SnS. In order to eliminate the influence of calcination temperature on the experimental results, the XRD patterns of sample SnS_2/GO after calcination under Ar atmosphere at different temperatues were collected (**Fig. S2**c). **Fig. S2**c shows that partial SnS_2 transformed to SnO_2 when calcined at 350 ℃ for 1 h, and SnS_2 phase was completely transformed into SnO_2 after

calcined at 550 ℃ for 1 h. In the as-prepared SnS_2/GO composite, GO contains rich oxygen-containing functional groups and there will be some adsorbed oxygen in the sample. Therefore, oxygen will still participate in the reaction during heat treatment in Ar gas. GO was reduced to RGO and SnS_2 was converted to SnO_2. The results indicate that the transformation from SnS_2 to SnS was caused by the phosphating effect of $NaH_2PO_2 \cdot H_2O$.

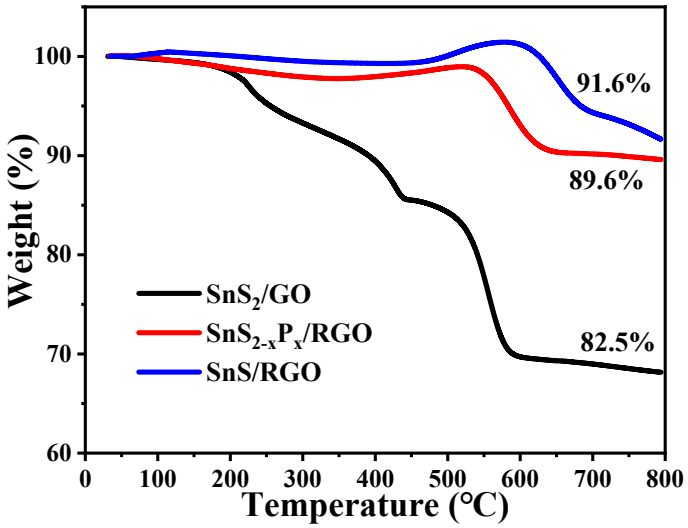

Fig. S3. Thermal analysis (TGA) of as-prepared samples

The weight loss below 100 ºC was due to the removal of absorbed water. The major weight loss in the range of 200-600 °C for SnS_2/GO is attributed to the combustion of RGO to CO_2 gas and the oxidation of SnS_2 to SO_2 gas when the sample was oxidized in air under high temperature. For $SnS_{2-x}P_x$/RGO and SnS/RGO, the weight increased between 400-700 °C was caused by the oxidation of doped phosphorus. Based on the fact that SnS_2, $SnS_{2-x}P_x$ and SnS were fully oxidized into SnO_2 at 800 °C in air and according to the weight loss in TGA result, the mass ratio of SnS_2 in the SnS_2/GO, $SnS_{2-x}P_x$/RGO and SnS/RGO composite is calculated as 82.5%, 89.6% and 91.6%, respectively.

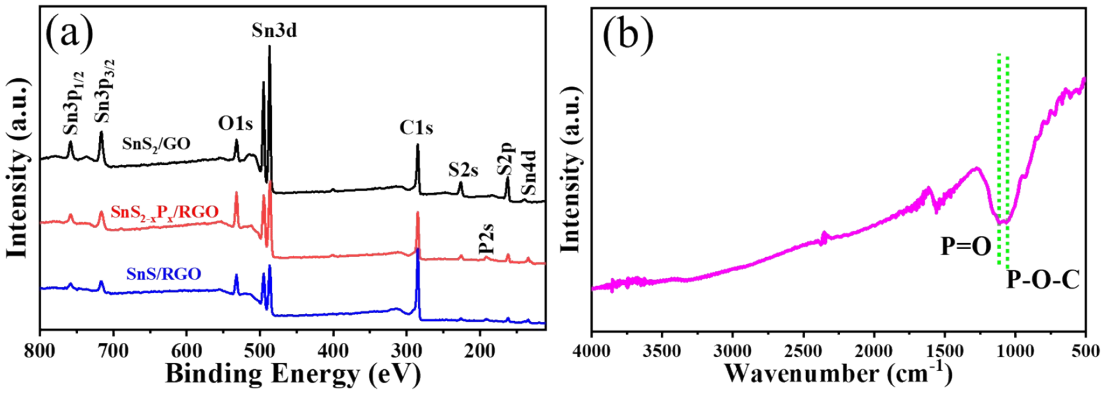

Fig. S4. (a) The XPS full survey spectra of the as-prepared samples and (b) FTIR spectrum of $SnS_{2-x}P_x$/RGO

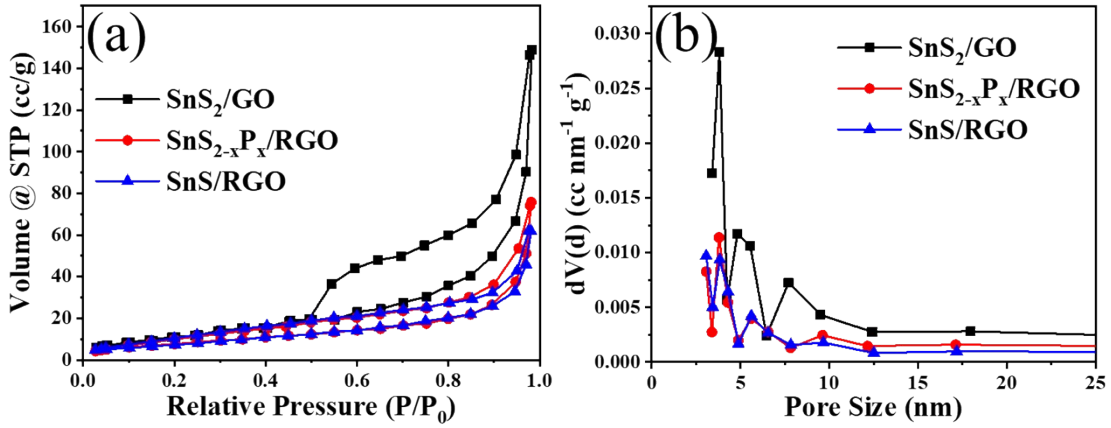

Fig. S5. (a) N_2 adsorption-desorption curves, and (b) BJH pore size distribution of the as-prepared samples.

The specific surface area and porosity of the as-prepared samples were investigated by N_2 adsorption-desorption measurements and the results are shown in **Fig. S5**. **Fig. S5**a displays that all these samples have obvious capillary condensation steps of type IV characteristics, indicating the presence of mesopores. The pore size distribution curves shown in **Fig. S5**b illustrate that all the three samples show wide distributed mesopore in between 2 and 10 nm. The BET specific surface area of SnS_2/GO, $SnS_{2-x}P_x$/RGO and SnS/RGO are 46.0, 19.5 and 19.4 $m^2\ g^{-1}$, respectively. The decrease in the surface area of samples $SnS_{2-x}P_x$/RGO and SnS/RGO can be attributed to the phosphating process and heat treatment.

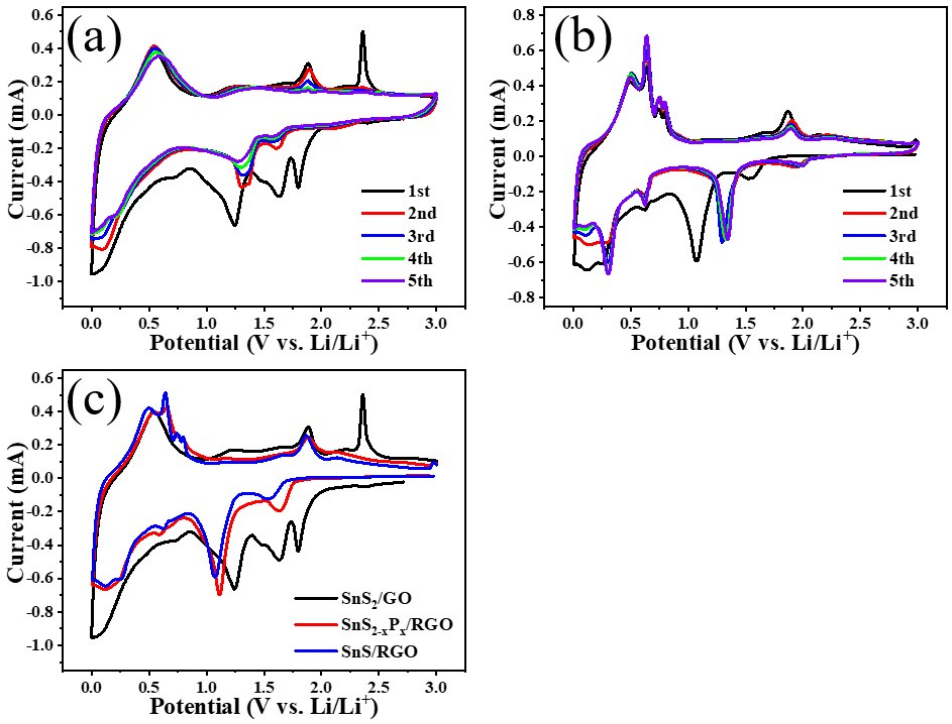

Fig. S6. CV curves of (a) SnS_2/GO and (a) SnS/RGO at a scan rate of 0.2 mV s^{-1}. (c) The comparation of the first cycle CV curves for the prepared samples.

CV curves of SnS_2/GO and SnS/RGO for the first five cycles were evaluated in the 0.01-3.00 V voltage range at 0.2 mV s^{-1}, as shown in **Fig. S6**. For the SnS_2/GO, as shown in **Fig. S6**a, during the initial CV cycle, the reduction peak at 1.79 V (vs. Li^+/Li) is mainly assigned to the intercalation of Li^+ into the SnS_2 layers to form Li_xSnS_2[3]. The peaks at 1.63 and 1.25 V are generally indexed to the transformation of Sn and Li_2S, as well as the formation of a solid electrolyte interface (SEI) film on the electrode surface at a low voltage. The reduction peak below 0.30 V (vs. Li^+/Li) in the first cathodic scan represents the reversible formation of Li_xSn alloy[4]. During the first reverse anodic process, the peak at 0.55 V is ascribed to the delithiation reaction of Li_xSn alloy, while another peak at 1.88 V possibly originated from the oxygenation of Sn nanoparticles at

higher potential in the charged state. The other oxidation peak at 2.36 V corresponds to lithium deintercalation from SnS_2 layers without phase decomposition[5].

For the SnS/RGO, as shown in **Fig. S6**b, in the initial cathodic scan, the reduction peak at 1.55 V correspond to the formation of Li_xSnS by Li-ion insertion into the SnS, and the peak at 1.08 V is attributed to the decomposition of Li_xSnS into metallic Sn and Li_2S, as well as the formation of SEI film[6]. The weak peak at 0.61 V and the peaks below 0.3 V are attributed to metal Sn and lithium ion alloying reaction to form Li_xSn[7]. In the first anodic scan, several peaks at 0.5, 0.64, 0.74 and 0.80 V are ascribed to the multi-step dealloying reaction of Li_xSn to Sn. The broad peak at 1.86 V is attributed to the oxidation of Sn to SnS.

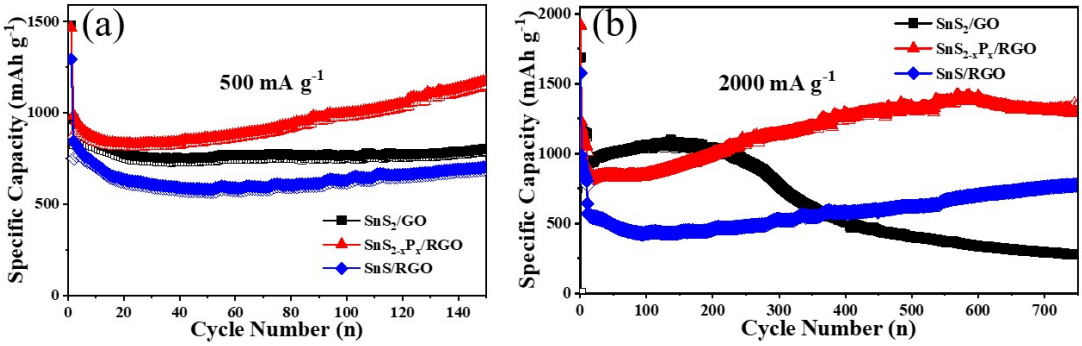

Fig. S7. Cycling performance of the as-prepared samples at (a) 500 mA g^{-1} and (b) 2000 mA g^{-1}.

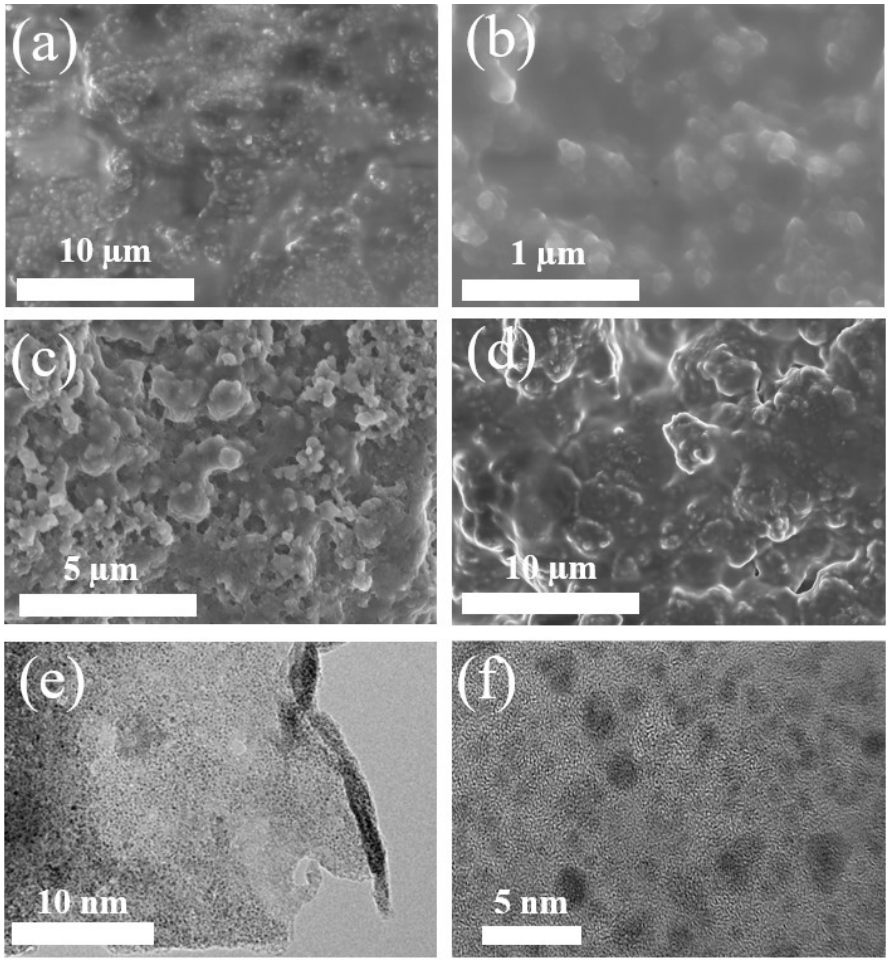

Fig. S8. SEM images of (a, b) $SnS_{2-x}P_x$/RGO, (c) SnS_2/GO, and (d) SnS/RGO electrodes after 300 cycles. TEM images of (e, f) $SnS_{2-x}P_x$/RGO after 300 cycles for LIBs.

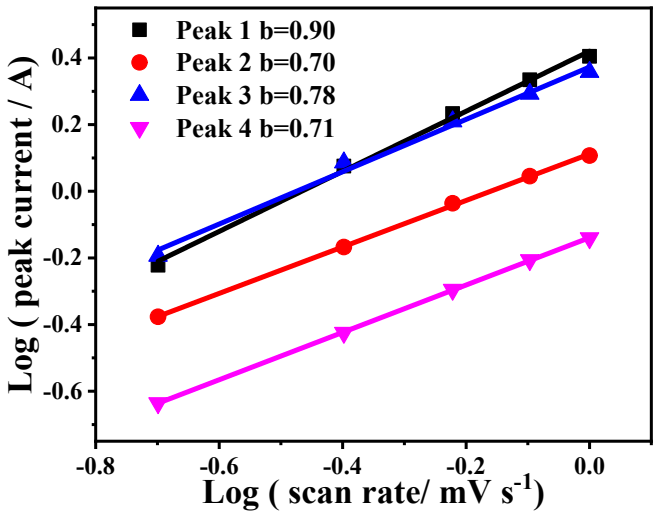

Fig. S9. *b*-values of $SnS_{2-x}P_x$/RGO derived from linear fitting relationship of log(*i*) *vs.* log(υ).

As displayed in **Fig. S9**, the b-values for peaks 1-4 are calculated to be 0.90, 0.70, 0.78 and 0.71, respectively, illustrating that the lithium storage behavior of $SnS_{2-x}P_x$/RGO is a mixed process of diffusion-controlled and pseudo-capacitive process, but the pseudo-capacitive contribution is the majority.

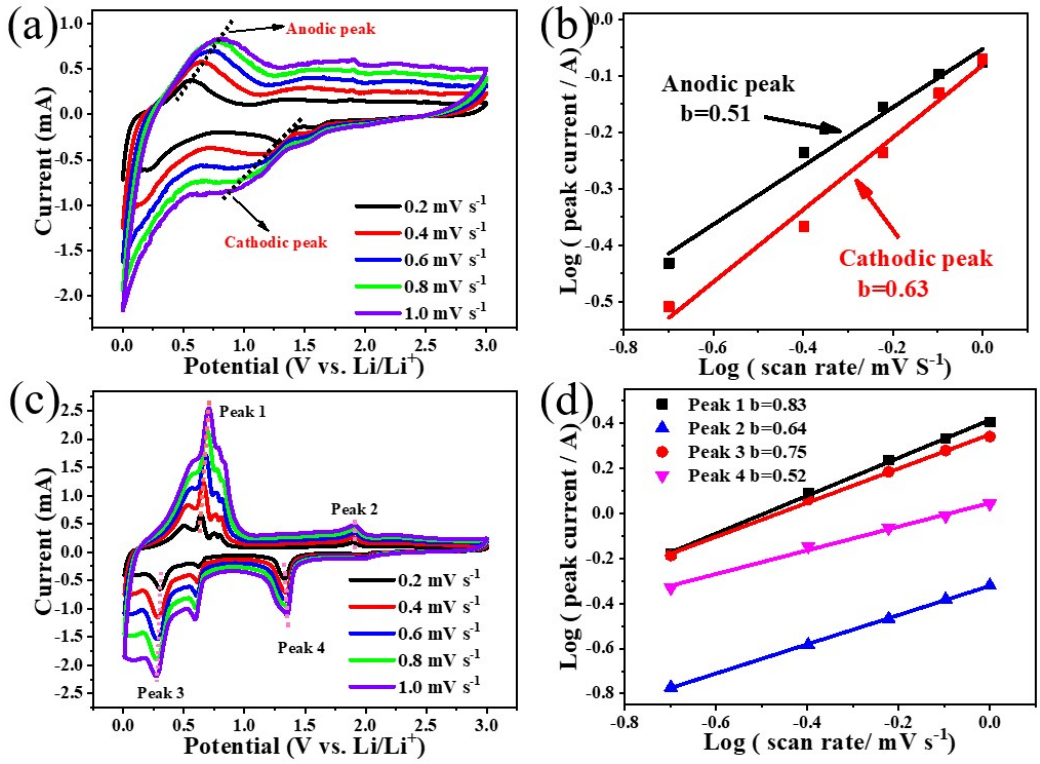

Fig. S10. CV curves at various scan rates and corresponding *b*-values derived from linear fitting relationship of log(*i*) *vs.* log(υ) for (a, b) SnS_2/GO and (c, d) SnS/RGO.

CV curves at various scan rates and corresponding b-values derived from linear fitting relationship of log(i) vs. log(v) for SnS_2/GO and SnS/RGO are displayed in **Fig. S10**. It shows that $SnS_{2-x}P_x$/RGO possessed higher b-value than that of SnS_2/GO and SnS/RGO, indicating that the contribution of pseudo-capacitive in the electrochemical behavior of $SnS_{2-x}P_x$/RGO electrode occupies a higher proportion.

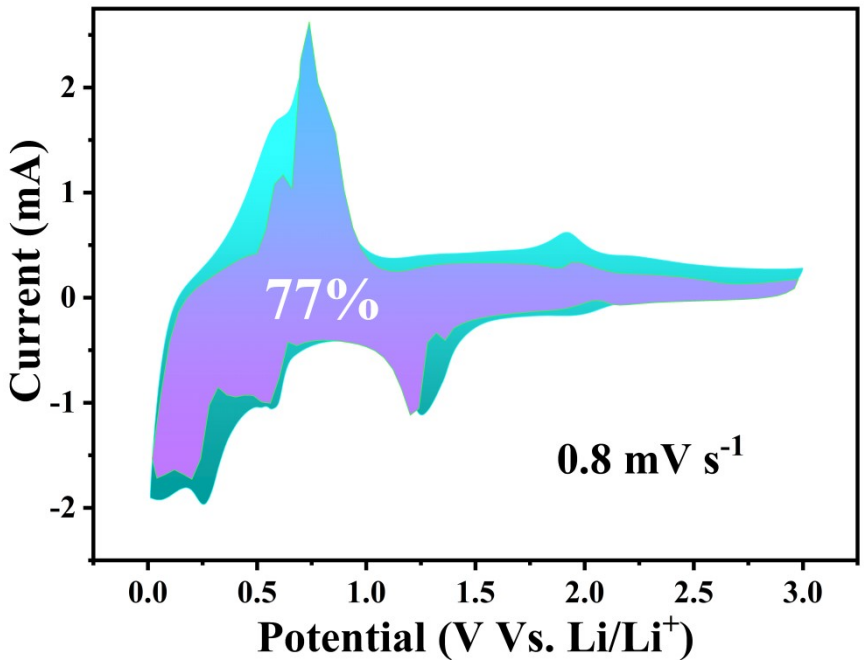

Fig. S11. CV profile of the capacitive contribution at a scan rate of 0.8 mV s^{-1} for $SnS_{2-x}P_x$/RGO

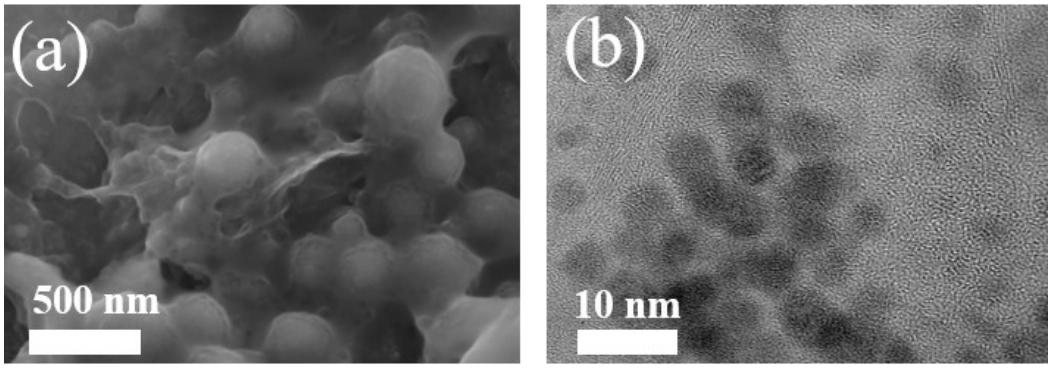

Fig. S12. SEM image (a) and (b) TEM image of $SnS_{2-x}P_x$/RGO after 300 cycles for SIBs.

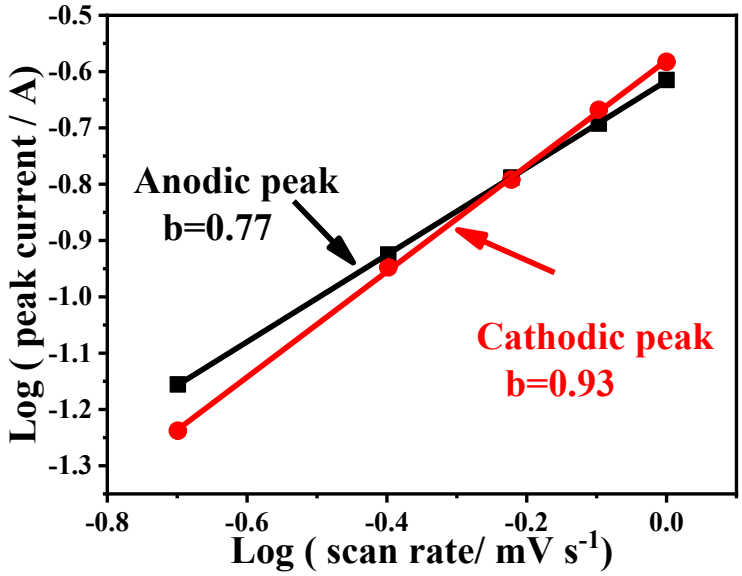

Fig. S13. Corresponding *b*-values derived from linear fitting relationship of log(*i*) *vs.* log(*υ*) for $SnS_{2-x}P_x$/RGO electrode in.

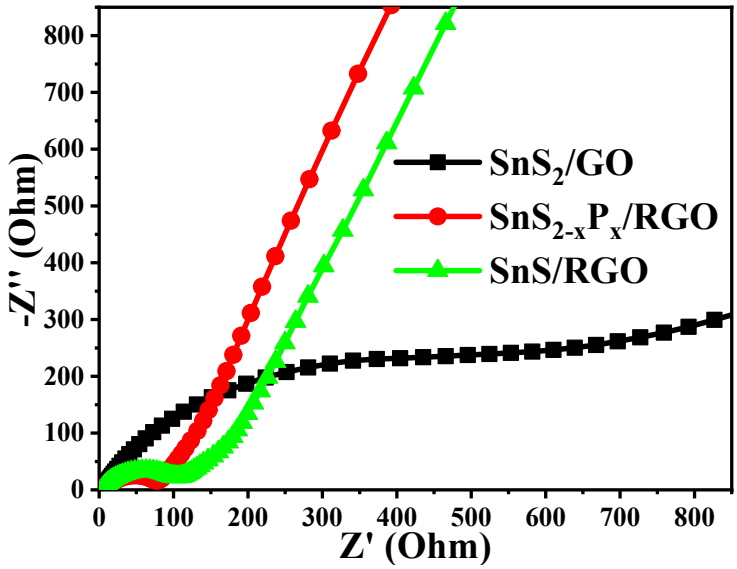

Fig. S14. (a) EIS curves of the as-prepared electrodes after 200 cycles for SIBs

Table S1. ICP results of $SnS_{2-x}P_x$/RGO

Elements	wt.%
Sn	48.1%
P	5.2%

Table S2. Comparison of performance for Sn-based materials as LIB anodes.

Materials	Current Density (mA g^{-1})	Cycle Number	Reversible Capacity (mA h g^{-1})	Ref.
SnS_2-CNT-CC	645	100	1250	Ref[1][8]
	2000	200	879	
SVR-SnS	2000	1200	765	Ref[2][9]
CNT/SnS_2@C	100	200	940	Ref[3][10]
c-SnS_2 NSA	1000	30	915	Ref[4][11]
SnS_2@C	100	200	1150	Ref[5][12]
	1000	500	676	
LEGr@SnS_2	300	200	664	Ref[6][13]
SnS_2@CNT	300	470	2733	Ref[7][14]
SnS/GNS	100	100	1016	Ref[8][15]
S-TC	100	100	426	Ref[9][16]
CC@$Sn_{0.9}Mo_{0.1}S_2$	1000	200	1950	Ref[10][17]
SnS_2/SnO	200	200	998	Ref[11][18]
H-TiO_2@SnS_2@PPy	2000	2000	508	Ref[12][19]
rGO/SnS_2/TiO_2	500	200	485	Ref[13][20]
SnS_2/rGO/SnS_2	1000	200	909	Ref[14][21]
SnS_2/NRGO	200	200	562	Ref[15][22]
Si@SnS_2-rGO	200	400	1480	Ref[16][23]
	3000	600	423	
SnS/S-GNS	100	100	803	Ref[17][24]
SnS_2/rGO	100	200	1010	Ref[18][25]
	1000	1000	910	
PPy@SnS_2@CNF	100	100	1165	Ref[19][26]
SnS/C	1000	300	535	Ref[20][27]
Ti_3C_2 MXene@C@SnS	1000	350	1050	Ref[21][6]
3D SnS/C	1000	1000	869	Ref[22][28]
SnS/C NFs	200	500	648	Ref[23][29]
	500	500	548	
SnS/PDDA-Ti_3C_2	100	100	646	Ref[24][30]
SnS@SC	1000	1000	922	Ref[25][31]
The SnS@G	100	200	1462	Ref[26][32]
	1000	500	1020	
$SnS_{2-x}P_x$/RGO	**500**	**150**	**1176**	**This Work**
	2000	**750**	**1289**	
	5000	**1000**	**587**	
	10000	**3000**	**337**	

Table S3. Comparison of Sn-Based Sulfide Anode Materials for SIBs

Materials	Current Density (mA g^{-1})	Cycle Number	Reversible Capacity (mA h g^{-1})	Ref.
hs-SnS_2	1000	1000	486	Ref[1][33]
3D-GNS/SnS_2	1000	1000	385	Ref[2][34]
SnS_2/NGS	500	200	453	Ref[3][35]
SnS_2/graphene	1000	600	330	Ref[4][36]
Co-SnS_2/CC	2000	200	800	Ref[5][37]
SnS_2/NiS_2@CC	500	100	588	Ref[6][38]
	2000	100	343	
SnS_2@CNSs	100	100	631	Ref[7][39]
CNT/SnS_2@C	100	200	605	Ref[8][10]
YDSC-SnS@NSC	1000	1500	284	Ref[9][40]
SnS@graphene	810	250	492	Ref[10][41]
	7290	250	308	
SMS/C NBs	5000	500	522	Ref[11][42]
SnS/SnS_2@CC	1000	1500	300	Ref[12][43]
SSC@SnS_2	500	1000	432	Ref[13][44]
	5000	1000	245	
SnS_2 QDs/Ti_3C_2	100	600	345	Ref[14][45]
SnS_2 NP/TiO_2@C	5000	600	338	Ref[15][46]
SnS_2@N, S-GA	20	50	527	Ref[16][47]
	50	100	360.5	
SnS_2/G	2500	150	338	Ref[17][48]
SnS_2/GCA	200	100	535	Ref[18][49]
SnS_2/rGO/SnS_2	100	100	1133	Ref[19][21]
GNS@SnS_2/SnS@C	100	100	475	Ref[20][50]
SnS_2@3DRGO	2000	700	401	Ref[21][51]
TiO_2@SnS_2@N-C	1000	600	293	Ref[22][52]
CoS_2/C@SnS_2	10000	3500	400	Ref[23][53]
SnS_2 NWAs	500	100	510	Ref[24][54]
SnS_2@C	200	200	626	Ref[25][55]
SnS_2@C	2000	500	440	Ref[26][56]
SnS2@C@rGO	1000	1000	274	Ref[27][57]
SnS_2/NSDC	500	200	380	Ref[28][58]
SnS_2/rGO	1000	1000	480	Ref[29][25]
SnS@C nanotubes	200	100	440	Ref[30][59]
SnS@CNT	1000	500	615	Ref[31][60]
SnS/C NFs	200	500	349	Ref[32][29]

SnS@SPC	100	100	400	Ref[33][61]
SnS/3DNG	2000	1000	509	Ref[34][62]
SnS/NG	1600	1200	600	Ref[35][63]
SnS QDs@NC	1000	500	172	Ref[36][64]
$SnS_{2-x}P_x$/RGO	**500**	**200**	**329**	**This work**
	1000	**4000**	**236**	
	2000	**4000**	**199**	

References:

1 Q. Tan, Z. Kong, X. Chen, L. Zhang, X. Hu, M. Mu, H. Sun, X. Shao, X. Guan, M. Gao and B. Xu, Synthesis of SnO_2/graphene composite anode materials for lithium-ion batteries, *Appl. Surf. Sci.*, 2019, **485**, 314-322.

2 H. Yao, P. Wang, Y. Gong, J. Zhang, X. Yu, L. Gu, C. Ouyang, Y. Yin, E. Hu, X. Yang, E. Stavitski, Y. Guo and L. Wan, Designing Air-Stable O3-Type Cathode Materials by Combined Structure Modulation for Na-Ion Batteries, *J. Am. Chem. Soc.*, 2017, **139**, 8440-8443.

3 X. Jiang, X. Yang, Y. Zhu, J. Shen, K. Fan and C. Li, In situ assembly of graphene sheets-supported SnS_2 nanoplates into 3D macroporous aerogels for high-performance lithium ion batteries, *J. Power Sources*, 2013, **237**, 178-186.

4 D. Gao, Y. Wang, Y. Liu, H. Sun, M. Wu and H. Zhang, Interfacial engineering of 0D/2D SnS_2 heterostructure onto nitrogen-doped graphene for boosted lithium storage capability, *J. Colloid Interf. Sci.*, 2019, **538**, 116-124.

5 J. Li, S. Han, C. Zhang, W. Wei, M. Gu and L. Meng, High-Performance and Reactivation Characteristics of High-Quality, Graphene-Supported SnS_2 Heterojunctions for a Lithium-Ion Battery Anode, *ACS Appl. Mater. Inter.*, 2019, **11**, 22314-22322.

6 H. Tang, R. Guo, M. Jiang, Y. Zhang, X. Lai, C. Cui, H. Xiao, S. Jiang, E. Ren and Q. Qin, Construction of Ti_3C_2 MXene@C@SnS with layered rock stratum structure for high-performance lithium storage, *J. Power Sources*, 2020, **462**, 228152.

7 B. Zhao, D. Song, Y. Ding, J. Wu, Z. Wang, Z. Chen, Y. Jiang and J. Zhang, Ultrastable Li-ion battery anodes by encapsulating SnS nanoparticles in sulfur-doped graphene bubble films, *Nanoscale*, 2020, **12**, 3941-3949.

8 Z. Syum, B. Venugopal, A. Sabbah, T. Billo, T. Chou, H. Wu, L. Chen and K. Chen, Superior lithium-ion storage performance of hierarchical tin disulfide and carbon nanotube-carbon cloth composites, *J. Power Sources*, 2021, **482**, 228923.

9 J. Zhang, D. Cao, Y. Wu, X. Cheng, W. Kang and J. Xu, Phase transformation and sulfur vacancy modulation of 2D layered tin sulfide nanoplates as highly durable anodes for pseudocapacitive lithium storage, *Chem. Eng. J.*, 2020, **392**, 123722.

10 B. Luo, Y. Hu, X. Zhu, T. Qiu, L. Zhi, M. Xiao, H. Zhang, M. Zou, A. Cao and L. Wang, Controllable growth of SnS_2 nanostructures on nanocarbon surfaces for lithium-ion and sodium-ion storage with high rate capability, *J. Mater. Chem. A*, 2018, **6**, 1462-1472.

11 Y. Wang, J. Zhou, J. Wu, F. Chen, P. Li, N. Han, W. Huang, Y. Liu, H. Ye, F. Zhao and Y. Li, Engineering SnS_2 nanosheet assemblies for enhanced electrochemical lithium and sodium ion

storage, *J. Mater. Chem. A*, 2017, **5**, 25618-25624.

12 J. Wang, H. Sun, H. Liu, D. Jin, R. Zhou and B. Wei, Edge-oriented SnS_2 nanosheet arrays on carbon paper as advanced binder-free anodes for Li-ion and Na-ion batteries, *J. Mater. Chem. A*, 2017, **5**, 23115-23122.

13 J. Li, S. Han, C. Zhang, W. Wei, M. Gu and L. Meng, High-Performance and Reactivation Characteristics of High-Quality, Graphene-Supported SnS_2 Heterojunctions for a Lithium-Ion Battery Anode, *ACS Appl. Mater. Inter.*, 2019, **11**, 22314-22322.

14 X. Jin, H. Huang, A. Wu, S. Gao, M. Lei, J. Zhao, X. Gao and G. Cao, Inverse Capacity Growth and Pocket Effect in SnS_2 Semifilled Carbon Nanotube Anode, *ACS Nano*, 2018, **12**, 8037-8047.

15 B. Zhao, F. Chen, Z. Wang, S. Huang, Y. Jiang and A. Z. Chen, Lithiation-assisted exfoliation and reduction of SnS_2 to SnS decorated on lithium-integrated graphene for efficient energy storage, *Nanoscale*, 2017, **9**, 17922-17932.

16 J. Li, L. Han, Y. Li, J. Li, G. Zhu, X. Zhang, T. Lu and L. Pan, MXene-decorated SnS_2/Sn_3S_4 hybrid as anode material for high-rate lithium-ion batteries, *Chem. Eng. J.*, 2020, **380**, 122590.

17 Qiang Chen, Fengqi Lu, Ying Xia, H. Wang and A. X. Kuang, Interlayer expansion of few-layered Mo-doped SnS_2 nanosheets grown on carbon cloth with excellent lithium storage performance for lithium ion batteries, *J. Mater. Chem. A*, **5**, 4075.

18 Y. Zhang, Z. Ma, D. Liu, S. Dou, J. Ma, M. Zhang, Z. Guo, R. Chen and S. Wang, p-Type SnO thin layers on n-type SnS_2 nanosheets with enriched surface defects and embedded charge transfer for lithium ion batteries, *J. Mater. Chem. A*, 2017, **5**, 512-518.

19 L. Wu, J. Zheng, L. Wang, X. Xiong, Y. Shao, G. Wang, J. Wang, S. Zhong and M. Wu, PPy-encapsulated SnS_2 Nanosheets Stabilized by Defects on a TiO_2 Support as a Durable Anode Material for Lithium-Ion Batteries, *Angew. Chem. Int. Edit.*, 2019, **58**, 811-815.

20 H. Wang, X. Zhao, X. Li, Z. Wang, C. Liu, Z. Lu, W. Zhang and G. Cao, rGO/SnS2/TiO2 heterostructured composite with dual-confinement for enhanced lithium-ion storage, *J. Mater. Chem. A*, 2017, **5**, 25056-25063.

21 Y. Jiang, D. Song, J. Wu, Z. Wang, S. Huang, Y. Xu, Z. Chen, B. Zhao and J. Zhang, Sandwich like SnS_2/Graphene/SnS_2 with Expanded Interlayer Distance as High-Rate Lithium/Sodium-Ion Battery Anode Materials, *ACS Nano*, 2019, **13**, 9100-9111.

22 D. H. Youn, S. K. Stauffer, P. Xiao, H. Park, Y. Nam, A. Dolocan, G. Henkelman, A. Heller and C. B. Mullins, Simple Synthesis of Nanocrystalline Tin Sulfide/N-Doped Reduced Graphene Oxide Composites as Lithium Ion Battery Anodes, *ACS Nano*, 2016, **10**, 10778-10788.

23 J. Dai, J. Liao, M. He, M. Yang, K. Wu and W. Yao, Si@SnS_2-Reduced Graphene Oxide Composite Anodes for High‐Capacity Lithium‐Ion Batteries, *ChemSusChem*, 2019, **12**, 5092-5098.

24 Y. Jiang, Y. Ding, F. Chen, Z. Wang, Y. Xu, S. Huang, Z. Chen, B. Zhao and J. Zhang, Structural phase transformation from SnS_2/reduced graphene oxide to SnS/sulfur-doped graphene and its lithium storage properties, *Nanoscale*, 2020, **12**, 1697-1706.

25 Z. Zhang, H. Zhao, J. Fang, X. Chang, Z. Li and L. Zhao, Tin Disulfide Nanosheets with Active-Site-Enriched Surface Interfacially Bonded on Reduced Graphene Oxide Sheets as Ultra-Robust Anode for Lithium and Sodium Storage, *ACS Appl. Mater. Inter.*, 2018, **10**, 28533-28540.

26 J. Wang, H. Sun, H. Liu, D. Jin, X. Liu, X. Li and F. Kang, Triaxial Nanocables of Conducting Polypyrrole@SnS_2@Carbon Nanofiber Enabling Significantly Enhanced Li-Ion Storage, *ACS Appl. Mater. Inter.*, 2018, **10**, 13581-13587.

27 C. Zhu, P. Kopold, W. Li, P. A. van Aken, J. Maier and Y. Yu, A General Strategy to Fabricate

Carbon-Coated 3D Porous Interconnected Metal Sulfides: Case Study of SnS/C Nanocomposite for High-Performance Lithium and Sodium Ion Batteries, *Adv. Sci.*, 2015, **2**, 1500200.

28 P. Xue, N. Wang, Y. Wang, Y. Zhang, Y. Liu, B. Tang, Z. Bai and S. Dou, Nanoconfined SnS in 3D interconnected macroporous carbon as durable anodes for lithium/sodium ion batteries, *Carbon*, 2018, **134**, 222-231.

29 J. Xia, L. Liu, S. Jamil, J. Xie, H. Yan, Y. Yuan, Y. Zhang, S. Nie, J. Pan, X. Wang and G. Cao, Free-standing SnS/C nanofiber anodes for ultralong cycle-life lithium-ion batteries and sodium-ion batteries, *Energy Storage Mater.*, 2019, **17**, 1-11.

30 J. Ai, Y. Lei, S. Yang, C. Lai and Q. Xu, SnS nanoparticles anchored on Ti3C2 nanosheets matrix via electrostatic attraction method as novel anode for lithium ion batteries, *Chem. Eng. J.*, 2019, **357**, 150-158.

31 Y. Cheng, Z. Wang, L. Chang, S. Wang, Q. Sun, Z. Yi and L. Wang, Sulfur-Mediated Interface Engineering Enables Fast SnS Nanosheet Anodes for Advanced Lithium/Sodium-Ion Batteries, *ACS Appl. Mater. Inter.*, 2020, **12**, 25786-25797.

32 B. Zhao, D. Song, Y. Ding, J. Wu, Z. Wang, Z. Chen, Y. Jiang and J. Zhang, Ultrastable Li-ion battery anodes by encapsulating SnS nanoparticles in sulfur-doped graphene bubble films, *Nanoscale*, 2020, **12**, 3941-3949.

33 J. Wang, J. Huang, S. Huang, H. Notohara, K. Urita, I. Moriguchi and M. Wei, Rational Design of Hierarchical SnS_2 Microspheres with S Vacancy for Enhanced Sodium Storage Performance, *ACS Sustain. Chem. Eng.*, 2020, **8**, 9519-9525.

34 Z. Sang, X. Yan, D. Su, H. Ji, S. Wang, S. X. Dou and J. Liang, A Flexible Film with SnS_2 Nanoparticles Chemically Anchored on 3D-Graphene Framework for High Areal Density and High Rate Sodium Storage, *Small*, 2020, **16**, 2001265.

35 S. Tao, D. Wu, S. Chen, B. Qian, W. Chu and L. Song, A versatile strategy for ultrathin SnS_2 nanosheets confined in a N-doped graphene sheet composite for high performance lithium and sodium-ion batteries, *Chem. Commun.*, 2018, **54**, 8379-8382.

36 X. Li, X. Sun, Z. Gao, X. Hu, R. Ling, S. Cai, C. Zheng and W. Hu, A Simple One-Pot Strategy for Synthesizing Ultrafine SnS_2 Nanoparticle/Graphene Composites as Anodes for Lithium/Sodium-Ion Batteries, *ChemSusChem*, 2018, **11**, 1549-1557.

37 L. Wang, Q. Zhao, Z. Wang, Y. Wu, X. Ma, Y. Zhu and C. Cao, Cobalt-doping SnS_2 nanosheets towards high-performance anodes for sodium ion batteries, *Nanoscale*, 2020, **12**, 248-255.

38 S. Guan, T. Wang, X. Fu, L. Fan and Z. Peng, Coherent SnS_2/NiS_2 hetero-nanosheet arrays with fast charge transfer for enhanced sodium-ion storage, *Appl. Surf. Sci.*, 2020, **508**, 145241.

39 Y. Liu, X. Yu, Y. Fang, X. Zhu, J. Bao, X. Zhou and X. W. D. Lou, Confining SnS_2 Ultrathin Nanosheets in Hollow Carbon Nanostructures for Efficient Capacitive Sodium Storage, *Joule*, 2018, **2**, 725-735.

40 M. Chen, Z. Zhang, L. Si, R. Wang and J. Cai, Engineering of Yolk-Double Shell Cube-like SnS@N-S Codoped Carbon as a High-Performance Anode for Li- and Na-Ion Batteries, *ACS Appl. Mater. Inter.*, 2019, **11**, 35050-35059.

41 T. Zhou, W. K. Pang, C. Zhang, J. Yang, Z. Chen, H. K. Liu and Z. Guo, Enhanced Sodium-Ion Battery Performance by Structural Phase Transition from Two-Dimensional Hexagonal-SnS_2 to Orthorhombic-SnS, *ACS Nano*, 2014, **8**, 8323-8333.

42 Y. Zhang, P. Zhu, L. Huang, J. Xie, S. Zhang, G. Cao and X. Zhao, Few-Layered SnS_2 on Few-Layered Reduced Graphene Oxide as Na-Ion Battery Anode with Ultralong Cycle Life and Superior

Rate Capability, *Adv. Funct. Mater.*, 2015, **25**, 481-489.

43 J. Lu, S. Zhao, S. Fan, Q. Lv, J. Li and R. Lv, Hierarchical SnS/SnS_2 heterostructures grown on carbon cloth as binder-free anode for superior sodium-ion storage, *Carbon*, 2019, **148**, 525-531.

44 Z. Yang, P. Zhang, J. Wang, Y. Yan, Y. Yu, Q. Wang and M. Liu, Hierarchical Carbon@SnS_2 Aerogel with "Skeleton/Skin" Architectures as a High-Capacity, High-Rate Capability and Long Cycle Life Anode for Sodium Ion Storage, *ACS Appl. Mater. Inter.*, 2018, **10**, 37434-37444.

45 J. Ding, C. Tang, G. Zhu, W. Sun, A. Du, F. He, M. Wu and H. Zhang, Integrating SnS_2 Quantum Dots with Nitrogen-Doped $Ti_3C_2T_x$ MXene Nanosheets for Robust Sodium Storage Performance, *ACS Appl. Energ. Mater.*, 2021, **4**, 846-854.

46 X. Hu, Q. Peng, T. Zeng, B. Shang, X. Jiao and G. Xi, Promotional role of nano TiO_2 for pomegranate-like SnS_2@C spheres toward enhanced sodium ion storage, *Chem. Eng. J.*, 2019, **363**, 213-223.

47 L. Fan, X. Li, X. Song, N. Hu, D. Xiong, A. Koo and X. Sun, Promising Dual-Doped Graphene Aerogel/SnS_2 Nanocrystal Building High Performance Sodium Ion Batteries, *ACS Appl. Mater. Inter.*, 2018, **10**, 2637-2648.

48 R. Thangavel, A. Samuthira Pandian, H. V. Ramasamy and Y. Lee, Rapidly Synthesized, Few-Layered Pseudocapacitive SnS_2 Anode for High-Power Sodium Ion Batteries, *ACS Appl. Mater. Inter.*, 2017, **9**, 40187-40196.

49 J. Cui, S. Yao, Z. Lu, J. Huang, W. G. Chong, F. Ciucci and J. Kim, Revealing Pseudocapacitive Mechanisms of Metal Dichalcogenide SnS_2/Graphene-CNT Aerogels for High-Energy Na Hybrid Capacitors, *Adv. Energy Mater.*, 2018, **8**, 1702488.

50 X. Su, D. Su, Z. Sang, X. Yan and J. Liang, Shielded SnS_2/SnS heterostructures on three-dimensional graphene framework for high-rate and stable sodium-ion storage, *Electrochim. Acta*, 2021, **372**, 137800.

51 J. Zheng, X. Xiong, G. Wang, Z. Lin, X. Ou, C. Yang and M. Liu, SnS_2 nanoparticles anchored on three-dimensional reduced graphene oxide as a durable anode for sodium ion batteries, *Chem. Eng. J.*, 2018, **339**, 78-84.

52 W. Ren, H. Zhang, C. Guan and C. Cheng, SnS_2 nanosheets arrays sandwiched by N-doped carbon and TiO_2 for high-performance Na-ion storage, *Green Energy Environ.*, 2018, **3**, 42-49.

53 L. Shi, D. Li, P. Yao, J. Yu, C. Li, B. Yang, C. Zhu and J. Xu, SnS_2 Nanosheets Coating on Nanohollow Cubic CoS_2/C for Ultralong Life and High Rate Capability Half/Full Sodium-Ion Batteries, *Small*, 2018, **14**, 1802716.

54 P. Zhou, X. Wang, W. Guan, D. Zhang, L. Fang and Y. Jiang, SnS_2 Nanowall Arrays toward High-Performance Sodium Storage, *ACS Appl. Mater. Inter.*, 2017, **9**, 6979-6987.

55 S. Li, Z. Zhao, C. Li, Z. Liu and D. Li, SnS_2@C Hollow Nanospheres with Robust Structural Stability as High-Performance Anodes for Sodium Ion Batteries, *Nano-Micro Lett.*, 2019, **11**.

56 Q. Sun, D. Li, L. Dai, Z. Liang and L. Ci, Structural Engineering of SnS_2 Encapsulated in Carbon Nanoboxes for High-Performance Sodium/Potassium-Ion Batteries Anodes, *Small*, 2020, **16**, 2005023.

57 D. Li, Q. Sun, Y. Zhang, L. Chen, Z. Wang, Z. Liang, P. Si and L. Ci, Surface-Confined SnS_2 @C@rGO as High‐Performance Anode Materials for Sodium- and Potassium-Ion Batteries, *ChemSusChem*, 2019, **12**, 2689-2700.

58 J. Xia, K. Jiang, J. Xie, S. Guo, L. Liu, Y. Zhang, S. Nie, Y. Yuan, H. Yan and X. Wang, Tin disulfide embedded in N-, S-doped carbon nanofibers as anode material for sodium-ion batteries,

Chem. Eng. J., 2019, **359**, 1244-1251.

59 P. He, Y. Fang, X. Yu and X. W. D. Lou, Hierarchical Nanotubes Constructed by Carbon-Coated Ultrathin SnS Nanosheets for Fast Capacitive Sodium Storage, *Angew. Chem. Int. Edit.*, 2017, **56**, 12202-12205.

60 T. H. T. Luu, D. L. Duong, T. H. Lee, D. T. Pham, R. Sahoo, G. Han, Y. Kim and Y. H. Lee, Monodispersed SnS nanoparticles anchored on carbon nanotubes for high-retention sodium-ion batteries, *J. Mater. Chem. A*, 2020, **8**, 7861-7869.

61 Y. Wang, Y. Zhang, J. Shi, A. Pan, F. Jiang, S. Liang and G. Cao, S-doped porous carbon confined SnS nanospheres with enhanced electrochemical performance for sodium-ion batteries, *J. Mater. Chem. A*, 2018, **6**, 18286-18292.

62 X. Xiong, C. Yang, G. Wang, Y. Lin, X. Ou, J. Wang, B. Zhao, M. Liu, Z. Lin and K. Huang, SnS nanoparticles electrostatically anchored on three-dimensional N-doped graphene as an active and durable anode for sodium-ion batteries, *Energ. Environ. Sci.*, 2017, **10**, 1757-1763.

63 L. Wang, X. Li, Z. Jin, Z. Liang, X. Peng, X. Ren, B. Gao, G. Feng, P. K. Chu and K. Huo, Spatially controlled synthesis of superlattice-like SnS/nitrogen-doped graphene hybrid nanobelts as high-rate and durable anode materials for sodium-ion batteries, *J. Mater. Chem. A*, 2019, **7**, 27475-27483.

64 G. K. Veerasubramani, M. Park, J. Choi and D. Kim, Ultrasmall SnS Quantum Dots Anchored onto Nitrogen-Enriched Carbon Nanospheres as an Advanced Anode Material for Sodium-Ion Batteries, *ACS Appl. Mater. Inter.*, 2020, **12**, 7114-7124.